A Direct Imaging Method for Inverse Scattering Using the Generalized Foldy–Lax Formulation

Gang Bao, Kai Huang, Peijun Li, and Hongkai Zhao

ABSTRACT. Consider the scattering of a time-harmonic plane wave incident on a two-scale heterogeneous medium, which consists of scatterers that are much smaller than the wavelength and extended scatterers that are comparable to the wavelength. In addition to the standard inverse obstacle scattering problem, i.e., to image the shape of extended scatterers as well as the location of the point scatterers where strong multiple scattering are present, there are a few other interesting issues such as imaging a target in a cluttered environment without resolving the clutters, and increasing the effective aperture by utilizing the multiple scattering between extended scatterers and point scatterers whose location are known. Some preliminary computational study will be given in this paper. To simulate the wave propagation in the heterogeneous medium with both point and extended scatterers, a generalized Foldy–Lax formulation and a physically based block Gauss–Seidel iterative method are used to solve the two-scale multiple scattering problem. Based on the singular value decomposition of the response matrix constructed from the far-field pattern, imaging functions are designed to visualize the location of the point scatterers and the shape of the extended obstacle scatterers. The method leads to a direct imaging algorithm which is simple and efficient since no direct solver or iteration is needed. The imaging functions are robust with respect to the measurement noise. Numerical experiments are presented for uniformly and randomly distributed point scatterers and multiple extended obstacle scatterers in both two- and three-dimensional cases.

1. Introduction

Scattering problems are about how an inhomogeneous medium scatters an incident wave field. The direct scattering problem is to determine the scattered field from the incident field and the differential equation governing the wave motion; the inverse scattering problem is to determine the nature of the inhomogeneity, such as
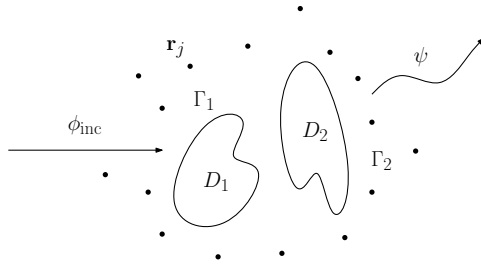
FIGURE 1. Schematic of problem geometry. The scattered wave ψ is generated from the incidence of a plane wave ϕ_{inc} on the heterogeneous medium consisting a group of point scatterers centered at $\mathbf{r}_j$ and an extended obstacle scatterer with possible multiple disjoint components represented by the domain D_k with boundary Γ_k.

location, geometry, and material property, from a knowledge of the scattered field. These problems have played a fundamental role in diverse scientific areas such as radar and sonar, geophysical exploration, medical imaging, near-field and nano-optics. This work is devoted to an inverse scattering problem where the considered scatterers are of two-scale nature: it consists of isotropic point scatterers and an extended obstacle scatterer with possible multiple disjoint components. "Isotropic point" refers that the scale of the scatterer is much smaller than the wavelength of the incident field so that the scatterer can be represented by a source point within it when scattering an incident wave; "extended" means that the scale of the obstacle scatterer is comparable with the wavelength of the incident field. More precisely, we consider the inverse scattering of a time-harmonic plane wave incident on the heterogeneous medium, and intend to reconstruct an image of the shape for the extended obstacle, represented by the boundary Γ of the domain D, and the location of the point scatterers at $\mathbf{r}_j$ from the far-field pattern of the scattered wave, as seen in Figure 1. The major motivation is to image a target in a cluttered environment. Here the target is modeled by an impenetrable obstacle and the cluttered environment is modeled by a set of isolated point scatterers surrounding the obstacle. In this work, we think that there are two contributions to the field of inverse scattering theory: (1) based on the generalized Foldy–Lax formulation, the proposed imaging functions can simultaneously show the shape of the extended obstacle scatterers and the location of the point scatterers; (2) computational study of the interaction and separation between point scatterers and extended scatterers in the imaging process.

The inverse scattering problem is challenging due to the inherently high non-linearity and, more seriously from the point of view of numerical computations, ill-posedness, i.e., small variations in the measured data can lead to large errors in the reconstruction. A number of methods have been proposed for solving the inverse scattering problem and they can be roughly categorized into two groups: nonlinear optimization based iterative methods and imaging based direct methods. The former methods are usually more quantitative and attempt to recover the properties or parameters as well as the geometry of the obstacle. On the other hand, they are more computationally intensive since iterations that requires solving a sequence

of direct and adjoint scattering problems are needed, see e.g., [**18**, **19**, **30**, **35**–**37**]. While the latter approaches are more qualitative and less computationally intensive, which give a characterization and/or visualization of the geometry by designing imaging functions which can highlight target boundary, see e.g., the MUSIC algorithm [**3**, **14**, **17**, **21**, **29**, **42**, **44**], the linear sampling method [**6**, **7**, **10**, **11**], the factorization method [**31**, **32**], the probe or enclosure method [**8**, **15**, **27**, **28**], and the method of singular sources [**40**, **41**]. In [**4**, **5**], a hybrid approach of combining the direct imaging method and the recursive linearization algorithm was used to solve an inverse medium scattering problem; a direct imaging method was adopted to generate an initial guess while the recursive linearization algorithm was applied to updates the approximations. We refer to the monograph [**33**] for a survey of all the non-iterative methods and the books [**12**, **13**] for comprehensive accounts of the direct and inverse scattering problems.

In this paper, we present a direct imaging method to simultaneously locate the point scatterers and reconstruct the shape of the extended scatterers. Specifically, we consider the inverse scattering problem of time-harmonic plane waves incident on the heterogeneous medium from a range of incident directions in two- or three-dimensional space. The far-field patterns of the scattered waves are recorded as data at various observation directions from plane incident waves sending at different directions of incidence. These measurements form the so-called response matrix which can be regarded as a discrete version of the scattering operator. Based on the singular value decomposition (SVD) of the response matrix, we design direct imaging functions to show the location of the point scatterers and the shape of the extended scatterers. The proposed direct imaging method is simple and efficient since no direct solver or iteration is needed. It can handle both full and limited aperture data. The imaging functions are robust with respect to the measurement noise. The method is closely related to the direct imaging methods in [**20**–**22**] and more recently in [**23**], where the medium was considered to be either point scatterers or extended obstacle, i.e., the medium is of the same scale nature. Here we consider the situation where both extended scatterers and a set of point scatterers with strong multiple scattering among them are present. To simulate the wave propagation in the heterogeneous medium with presence of both types of scatterers, it is required to accurately solve the forward scattering problem where the multiple scattering occurs among all the scatterers. We mention that the classic Foldy–Lax formulation is efficient to solve the multiple scattering of scalar waves by a distribution of small isotropic scatterers [**16**, **38**], and boundary integral equation methods have been considered as appropriate approaches for solving the scattering of acoustic or electromagnetic waves by bounded obstacles [**36**, **37**]. The generalized Foldy–Lax formulations have been developed in [**24**–**26**] to solve the multiple scattering problem when both the point scatterers and the extended obstacles are present. We briefly introduce the generalized Foldy–Lax formulation in the context of the inverse obstacle scattering and present a physically motivated block Gauss–Seidel iterative method. The detailed discussion may be found in [**25**] on the uniqueness and existence of the solution for the generalized Foldy–Lax formulation, as well as the convergence analysis of the block Gauss–Seidel iterative method. We refer to the proceedings [**2**] for an overview of mathematical and statistical methods for scattering problems related imaging.

The outline of the paper is as follows. In Section 2, the classical Foldy–Lax formulation is briefly reviewed for the scattered field from the interaction among a set of well-separated point scatterers; based on combined single- and double-layer potential representations, a uniquely solvable boundary integral equation is introduced for the obstacle scattering problem, where the scatterer is modeled as a wavelength comparable or an extended sound-soft obstacle; a generalized Foldy–Lax formulation is described for the multiple scattering problem involving both small-scale point scatterers and extended scatterers; and a block Gauss–Seidel iterative method is given to solve the coupled scattering system. Section 3 is devoted to the derivation of the far-field patterns and the construction of the imaging functions for three types of scatterers: point scatterers, extended obstacle scatterers, and mixed scatterers with both point and extended scatterers. Numerical results are shown in Section 4 for uniformly and randomly distributed point scatterers and multiple extended obstacle scatterers in both two- and three-dimensional cases. The paper is concluded with comments and directions for future work in Section 5.

2. Generalized Foldy–Lax formulation

In this section, we briefly introduce the original Foldy-Lax formulation for the point scatterers; the boundary integral equation for the extended obstacle scattering problem; the generalized Foldy–Lax formulation for the multiple scattering problem involving both extended obstacle scatterers and a set of isotropic point scatterers; and an efficient physically motivated block Gauss–Seidel algorithm for solving the coupled scattering system.

2.1. Foldy–Lax formulation for point scatterers. We briefly introduce the original Foldy–Lax formulation to model the scattering of isotropic point scatterers, which are named as delta-potentials in Rudnick and Ueberschär [**43**], and Colin de Verdière[**9**]. We refer to the book by Martin [**39**] for detailed discussions on the Foldy–Lax formulation.

Consider a collection of m separated isotropic point scatterers, which are represented by point sources located at $\mathbf{r}_1, \ldots, \mathbf{r}_m$. Let ϕ_{inc} be the plane incident wave, given explicitly

$$(2.1) \qquad \phi_{\text{inc}}(\mathbf{r}) = e^{\mathrm{i}\kappa \mathbf{r}\cdot\mathbf{d}} \quad \text{in } \mathbb{R}^\mu,$$

where i is the imaginary unit, κ is the wavenumber, $\mathbf{d} \in \mathbb{S}^{\mu-1}$ is the propagation direction defined on the unit sphere, and the dimension $\mu = 2, 3$. Clearly, the incident field satisfies the Helmholtz equation in the free space

$$(2.2) \qquad \Delta\phi_{\text{inc}} + \kappa^2\phi_{\text{inc}} = 0 \quad \text{in } \mathbb{R}^\mu.$$

The total field is represented as the sum of the incident field and the scattered field

$$(2.3) \qquad \phi(\mathbf{r}) = \phi_{\text{inc}}(\mathbf{r}) + \sum_{j=1}^{m} \sigma_j \phi_j G(\mathbf{r}, \mathbf{r}_j),$$

where σ_j is referred to as the scattering coefficient for the j-th point scatterer, ϕ_j is the external field acting on the j-th point scatterer, and G is the free-space Green's

function given as

$$
G(\mathbf{r}, \mathbf{r}') = \begin{cases} \dfrac{\mathrm{i}}{4} H_0^{(1)}(\kappa|\mathbf{r} - \mathbf{r}'|), & \text{for } \mu = 2, \\[2ex] \dfrac{1}{4\pi} \dfrac{e^{\mathrm{i}\kappa|\mathbf{r}-\mathbf{r}'|}}{|\mathbf{r} - \mathbf{r}'|}, & \text{for } \mu = 3. \end{cases}
$$

Here $H_0^{(1)}$ is the Hankel function of the first kind with order zero.

Evaluating (2.3) at $\mathbf{r}_i$ and excluding the self-interaction yield a linear system of algebraic equation for $\phi_j, j = 1, \ldots, m$:

$$
(2.4) \qquad \phi_i - \sum_{\substack{j=1 \\ j \neq i}}^{m} \sigma_j \phi_j G(\mathbf{r}_i, \mathbf{r}_j) = \phi_{\mathrm{inc}}(\mathbf{r}_i),
$$

which is known as the Foldy–Lax formulation. Once (2.4) is solved, the scattered field can be computed as

$$
(2.5) \qquad \psi(\mathbf{r}) = \sum_{j=1}^{m} \sigma_j \phi_j G(\mathbf{r}, \mathbf{r}_j).
$$

2.2. Boundary integral formulation for extended obstacle scatterers. This section is concerned with a brief introduction to the method of the boundary integral equation for solving the extended obstacle scattering problem. We refer to the monograph by Colton and Kress [**12**] for a comprehensive account of the boundary integral equation methods for solving the obstacle scattering problem.

We assume that the extended obstacle scatterer is represented by the domain D with boundary Γ, which is the open complement of an unbounded domain of class C^2, i.e., scattering from more than one component is included in our analysis.

Consider the Helmholtz equation

$$
(2.6) \qquad \Delta\phi + \kappa^2\phi = 0 \quad \text{in } \mathbb{R}^\mu \setminus \overline{D},
$$

along with the sound-soft boundary condition

$$
(2.7) \qquad \phi = 0 \quad \text{on } \Gamma,
$$

where ϕ is the total field and κ is the wavenumber.

The extended obstacle scatterer is illuminated by the plane incident wave given in (2.1). The total field ϕ consists of the incident field ϕ_{inc} and the scattered field ψ:

$$
(2.8) \qquad \phi = \phi_{\mathrm{inc}} + \psi.
$$

It follows from (2.2) and (2.6)–(2.8) that the scattered field satisfies

$$
(2.9) \qquad \Delta\psi + \kappa^2\psi = 0 \quad \text{in } \mathbb{R}^\mu \setminus \overline{D},
$$

together with the boundary condition

$$
(2.10) \qquad \psi = -\phi_{\mathrm{inc}} \quad \text{on } \Gamma.
$$

In addition, the scattered field is required to satisfy the Sommerfeld radiation condition

$$
(2.11) \qquad \lim_{\rho \to \infty} \rho^{\frac{\mu-1}{2}} \left(\frac{\partial\psi}{\partial\rho} - \mathrm{i}\kappa\psi \right) = 0, \quad \rho = |\mathbf{r}|.
$$

Based on the Green's representation theorem, it can be shown that the scattered field has the integral representation in terms of the normal derivative of the total field:

$$(2.12) \qquad \psi(\mathbf{r}) = -\int_{\Gamma} G(\mathbf{r}, \mathbf{r}') \partial_{\mathbf{n}'} \phi(\mathbf{r}') ds(\mathbf{r}'), \quad \mathbf{r} \in \mathbb{R}^{\mu} \setminus \overline{D},$$

where $\mathbf{n}$ is the unit outward normal on Γ and is assumed to be directed into the exterior of D.

To compute the scattered field, it is required to determine $\partial_{\mathbf{n}} \phi$ on Γ. We adopt the following uniquely solvable boundary integral equation:

$$(2.13) \quad \frac{1}{2} \partial_{\mathbf{n}} \phi(\mathbf{r}) + \int_{\Gamma} \left[\partial_{\mathbf{n}} G(\mathbf{r}, \mathbf{r}') - i\eta G(\mathbf{r}, \mathbf{r}') \right] \partial_{\mathbf{n}'} \phi(\mathbf{r}') ds(\mathbf{r}') = (\partial_{\mathbf{n}} - i\eta)\phi_{\text{inc}}(\mathbf{r}),$$

where η is the coupling parameter. We refer to Kress [34] for an investigation on the proper choice of the coupling parameter η with respect to the condition number of the coefficient matrix for the integral equation.

REMARK 2.1. If the extended obstacle scatterer is consisted of n disjoint components, i.e., $\Gamma = \Gamma_1 \cup \cdots \cup \Gamma_n$, $\Gamma_k \cap \Gamma_{k'} = \emptyset$, $k \neq k'$, then the boundary integral equation (2.13) can be written as

$$(2.14) \quad \frac{1}{2}\varphi(\mathbf{r}) + \sum_{k=1}^{n} \int_{\Gamma_k} \left[\partial_{\mathbf{n}} G(\mathbf{r}, \mathbf{r}') - i\eta G(\mathbf{r}, \mathbf{r}') \right] \varphi_k(\mathbf{r}') ds(\mathbf{r}') = (\partial_{\mathbf{n}} - i\eta)\phi_{\text{inc}}(\mathbf{r}),$$

where $\varphi(\mathbf{r}) = \partial_{\mathbf{n}} \phi(\mathbf{r})$ and $\varphi_k(\mathbf{r}) = \varphi(\mathbf{r})|_{\mathbf{r} \in \Gamma_k}$.

2.3. Generalized Foldy–Lax formulation. This section introduces the generalized Foldy–Lax formulation for the multiple scattering among the extended obstacle scatterer and the group of point scatterers. The existence and uniqueness of the solution for the formulation may be found in [25].

Viewing the external field acting on the point scatterers as point sources for the extended obstacle scatterer, we consider the equation for the total field

$$(2.15) \qquad \Delta\phi + \kappa^2 \phi = -\sum_{j=1}^{m} \sigma_j \phi_j \delta(\mathbf{r} - \mathbf{r}_j) \quad \text{in } \mathbb{R}^{\mu} \setminus \overline{D},$$

along with the sound-soft boundary condition

$$(2.16) \qquad \phi = 0 \quad \text{on } \Gamma,$$

where ϕ_j is again the external field acting on the j-th point scatterer and δ is the Dirac delta function. Subtracting the incident field from the total field, we may obtain the equation for the scattered field

$$(2.17) \qquad \Delta\psi + \kappa^2 \psi = -\sum_{j=1}^{m} \sigma_j \phi_j \delta(\mathbf{r} - \mathbf{r}_j) \quad \text{in } \mathbb{R}^{\mu} \setminus \overline{D}.$$

The scattered field is also required to satisfy the Sommerfeld radiation condition

$$(2.18) \qquad \lim_{\rho \to \infty} \rho^{\frac{\mu-1}{2}} \left(\frac{\partial \psi}{\partial \rho} - i\kappa\psi \right) = 0, \quad \rho = |\mathbf{r}|.$$

Similarly, it can be verified that the scattered field has the representation given in terms of the normal derivative of the total field and the external fields acting on

the point scatterers:

$$(2.19) \qquad \psi(\mathbf{r}) = \sum_{j=1}^{m} \sigma_j \phi_j G(\mathbf{r}, \mathbf{r}_j) - \int_{\Gamma} G(\mathbf{r}, \mathbf{r}') \partial_{\mathbf{n}'} \phi(\mathbf{r}') ds(\mathbf{r}'), \quad \mathbf{r} \in \mathbb{R}^{\mu} \setminus \overline{D}.$$

Adding the incident field on both sides of (2.19) yields

$$(2.20) \ \phi(\mathbf{r}) = \phi_{\text{inc}}(\mathbf{r}) + \sum_{j=1}^{m} \sigma_j \phi_j G(\mathbf{r}, \mathbf{r}_j) - \int_{\Gamma} G(\mathbf{r}, \mathbf{r}') \partial_{\mathbf{n}'} \phi(\mathbf{r}') ds(\mathbf{r}'), \quad \mathbf{r} \in \mathbb{R}^{\mu} \setminus \overline{D}.$$

To compute the scattered field, it is required to compute $\partial_{\mathbf{n}} \phi$ and $\phi_j, j = 1, \ldots, m$.

Evaluating (2.20) on both sides at $\mathbf{r}_i$ and excluding the self-interaction for the point scatterers give

$$(2.21) \qquad \phi_i = \phi_{\text{inc}}(\mathbf{r}_i) + \sum_{\substack{j=1 \\ j \neq i}}^{m} \sigma_j \phi_j G(\mathbf{r}_i, \mathbf{r}_j) - \int_{\Gamma} G(\mathbf{r}_i, \mathbf{r}') \partial_{\mathbf{n}'} \phi(\mathbf{r}') ds(\mathbf{r}').$$

Using the jump relation for the single-layer and double-layer potentials and taking the normal derivative, we may obtain a boundary integral equation on Γ:

$$\frac{1}{2} \partial_{\mathbf{n}} \phi(\mathbf{r}) = (\partial_{\mathbf{n}} - \mathrm{i}\eta) \, \phi_{\text{inc}}(\mathbf{r}) + \sum_{j=1}^{m} \sigma_j \phi_j \partial_{\mathbf{n}} G(\mathbf{r}, \mathbf{r}_j)$$

$$(2.22) \qquad\qquad - \int_{\Gamma} [\partial_{\mathbf{n}} G(\mathbf{r}, \mathbf{r}') - \mathrm{i}\eta G(\mathbf{r}, \mathbf{r}')] \, \partial_{\mathbf{n}'} \phi(\mathbf{r}') ds(\mathbf{r}').$$

The coupled scattering system (2.21) and (2.22) form the self-consistent generalized Foldy–Lax formulation, which take full account of the multiple scattering among the extended obstacle and the point scatterers.

REMARK 2.2. If the extended obstacle scatterer is consisted of n multiple components, then the generalized Foldy–Lax formulation can be written as the following coupled system

$$(2.23) \qquad \phi_i = \phi_{\text{inc}}(\mathbf{r}_i) + \sum_{\substack{j=1 \\ j \neq i}}^{m} \sigma_j \phi_j G(\mathbf{r}_i, \mathbf{r}_j) - \sum_{k=1}^{n} \int_{\Gamma_k} G(\mathbf{r}_i, \mathbf{r}') \varphi_k(\mathbf{r}') ds(\mathbf{r}'),$$

$$\frac{1}{2} \varphi(\mathbf{r}) = (\partial_{\mathbf{n}} - \mathrm{i}\eta) \, \phi_{\text{inc}}(\mathbf{r}) + \sum_{j=1}^{m} \sigma_j \phi_j \partial_{\mathbf{n}} G(\mathbf{r}, \mathbf{r}_j)$$

$$(2.24) \qquad\qquad - \sum_{k=1}^{n} \int_{\Gamma_k} [\partial_{\mathbf{n}} G(\mathbf{r}, \mathbf{r}') - \mathrm{i}\eta G(\mathbf{r}, \mathbf{r}')] \, \varphi_k(\mathbf{r}') ds(\mathbf{r}'),$$

where $\varphi(\mathbf{r}) = \partial_{\mathbf{n}} \phi(\mathbf{r})$ and $\varphi_k(\mathbf{r}) = \varphi(\mathbf{r})|_{\mathbf{r} \in \Gamma_k}$.

2.4. Block Gauss-Seidel iteration. We briefly describe an efficient physically motivated block Gauss–Seidel iterative method to solve the generalized Foldy–Lax formulation (2.23)–(2.24). The convergence analysis may be found in [**25**].

A block Gauss–Seidel iterative algorithm proceeds as follows: Let $\left(\phi_1^{(0)}, \ldots, \right.$ $\left. \phi_m^{(0)} \right)^{\top} = (0, \ldots, 0)^{\top}$ and $\varphi_k^{(0)}(\mathbf{r}) = 0$ for $k = 1, \ldots, n$, define $\left(\phi_1^{(\nu)}, \ldots, \phi_m^{(\nu)} \right)^{\top}$ and

$\varphi_k^{(\nu)}$ for $\nu \geq 1$ by the solutions of the following system of equations

$$(2.25) \quad \phi_i^{(\nu)} - \sum_{\substack{j=1 \\ j \neq i}}^{m} \sigma_j \phi_j^{(\nu)} G(\mathbf{r}_i, \mathbf{r}_j) = \phi_{\text{inc}}(\mathbf{r}_i) - \sum_{k=1}^{n} \int_{\Gamma_k} G(\mathbf{r}_i, \mathbf{r}') \varphi_k^{(\nu-1)}(\mathbf{r}') ds(\mathbf{r}')$$

and

$$\frac{1}{2} \varphi_k^{(\nu)}(\mathbf{r}) + \int_{\Gamma_k} [\partial_{\mathbf{n}} G(\mathbf{r}, \mathbf{r}') - \mathrm{i}\eta G(\mathbf{r}, \mathbf{r}')] \varphi_k^{(\nu)}(\mathbf{r}') ds(\mathbf{r}') = (\partial_{\mathbf{n}} - \mathrm{i}\eta) \phi_{\text{inc}}(\mathbf{r})$$

$$+ \sum_{j=1}^{m} \sigma_j \phi_j^{(\nu)} \partial_{\mathbf{n}} G(\mathbf{r}, \mathbf{r}_j) - \sum_{j=1}^{k-1} \int_{\Gamma_j} [\partial_{\mathbf{n}} G(\mathbf{r}, \mathbf{r}') - \mathrm{i}\eta G(\mathbf{r}, \mathbf{r}')] \varphi_j^{(\nu)}(\mathbf{r}') ds(\mathbf{r}')$$

$$(2.26) \qquad\qquad - \sum_{j=k+1}^{n} \int_{\Gamma_j} [\partial_{\mathbf{n}} G(\mathbf{r}, \mathbf{r}') - \mathrm{i}\eta G(\mathbf{r}, \mathbf{r}')] \varphi_j^{(\nu-1)}(\mathbf{r}') ds(\mathbf{r}'),$$

for $k = 1, \ldots, n$.

As can be seen from the block Gauss–Seidel iterative algorithm, it is only required to solve a linear system of algebraic equations and a boundary integral equation for a single obstacle at each step of iteration.

3. Response matrix

In this section, we introduce the response matrix and design imaging functions to characterize the location of the point scatterers and the geometry of the extended obstacle scatterer. The imaging function as proposed in [**23**] is made of those singular vectors corresponding to dominant singular values of the response matrix, which is constructed from the far-field pattern of the scattered waves.

3.1. Far-field pattern. The far-field pattern of scattered wave plays a fundamental role in the inverse scattering theory due to the fact that it induces the important geometrical and physical information, e.g., location, shape, and the impedance of the boundary, on the scattering object. More specifically, given an incident field with incident direction $\mathbf{d}$, if ψ is the scattered field, then ψ has the asymptotic behavior

$$(3.1) \qquad \psi(\mathbf{r}, \mathbf{d}) = \frac{e^{\mathrm{i}\kappa|\mathbf{r}|}}{|\mathbf{r}|^{\frac{\mu-1}{2}}} \left[\psi_\infty(\hat{\mathbf{r}}, \mathbf{d}) + O(|\mathbf{r}|)^{-1} \right] \quad \text{as } |\mathbf{r}| \to \infty$$

uniformly in all directions $\hat{\mathbf{r}} = \mathbf{r}/|\mathbf{r}|$, where the function ψ_∞ is called as the far-field pattern of the scattered field ψ, and $\hat{\mathbf{r}} \in \mathbb{S}^{\mu-1}$ is known as the observation direction.

Recall the asymptotic behavior for the Hankel function for large arguments

$$H_0^{(1)}(z) = \sqrt{\frac{2}{\pi z}} \, e^{\mathrm{i}\left(z - \frac{\pi}{4}\right)} \left[1 + O(z^{-1}) \right]$$

and the following identity

$$|\mathbf{r} - \mathbf{r}'| = \sqrt{|\mathbf{r}|^2 - 2\mathbf{r} \cdot \mathbf{r}' + |\mathbf{r}'|^2} = |\mathbf{r}| - \hat{\mathbf{r}} \cdot \mathbf{r}' + O(|\mathbf{r}|^{-1}) \quad \text{as } |\mathbf{r}| \to \infty.$$

Following (3.1) and (2.5), we obtain the far-field pattern of the scattered field for the scattering problem of a set of m point scatterers:

$$(3.2) \qquad\qquad \psi_{\infty, \text{FL}}(\hat{\mathbf{r}}, \mathbf{d}) = \gamma \sum_{j=1}^{m} \sigma_j \phi_j(\mathbf{d}) e^{-\mathrm{i}\kappa \hat{\mathbf{r}} \cdot \mathbf{r}_j},$$

where the constant γ is defined as

$$\gamma = \begin{cases} \dfrac{e^{\mathrm{i}\frac{\pi}{4}}}{\sqrt{8\pi\kappa}}, & \text{for } \mu = 2, \\[2ex] \dfrac{1}{4\pi}, & \text{for } \mu = 3. \end{cases}$$

It follows from the integral representation of the scattered field (2.12) and the asymptotic expansion of Green's function that the far-field pattern for the extended obstacle scatterer is given by

$$(3.3) \qquad \psi_{\infty,\,\mathrm{E}}(\hat{\mathbf{r}}, \mathbf{d}) = -\gamma \int_{\Gamma} \partial_{\mathbf{n}'}\phi(\mathbf{r}'; \mathbf{d})e^{-\mathrm{i}\kappa\hat{\mathbf{r}}\cdot\mathbf{r}'}\, ds(\mathbf{r}').$$

Based on the integral equation representation (2.19) for the multiple scattering problem and the asymptotic behavior for Green's function, we may also obtain the far-field pattern of the scattered field for the generalized Foldy–Lax formulation

$$(3.4) \qquad \psi_{\infty,\,\mathrm{GFL}}(\hat{\mathbf{r}}, \mathbf{d}) = \gamma \left[\sum_{j=1}^{m} \sigma_j \phi_j(\mathbf{d})e^{-\mathrm{i}\kappa\hat{\mathbf{r}}\cdot\mathbf{r}_j} - \int_{\Gamma} \partial_{\mathbf{n}'}\phi(\mathbf{r}'; \mathbf{d})e^{-\mathrm{i}\kappa\hat{\mathbf{r}}\cdot\mathbf{r}'}\, ds(\mathbf{r}') \right].$$

REMARK 3.1. For the extended obstacle scatterer with n disjoint components, the far-field patterns for the extended obstacle scatterer and the generalized Foldy–Lax formulation can be written as

$$\psi_{\infty,\,\mathrm{E}}(\hat{\mathbf{r}}, \mathbf{d}) = -\gamma \sum_{k=1}^{n} \int_{\Gamma_k} \partial_{\mathbf{n}'}\phi(\mathbf{r}'; \mathbf{d})e^{-\mathrm{i}\kappa\hat{\mathbf{r}}\cdot\mathbf{r}'}\, ds(\mathbf{r}').$$

and

$$\psi_{\infty,\,\mathrm{GFL}}(\hat{\mathbf{r}}, \mathbf{d}) = \gamma \left[\sum_{j=1}^{m} \sigma_j \phi_j(\mathbf{d})e^{-\mathrm{i}\kappa\hat{\mathbf{r}}\cdot\mathbf{r}_j} - \sum_{k=1}^{n} \int_{\Gamma_k} \partial_{\mathbf{n}'}\phi(\mathbf{r}'; \mathbf{d})e^{-\mathrm{i}\kappa\hat{\mathbf{r}}\cdot\mathbf{r}'}\, ds(\mathbf{r}') \right].$$

These far-field patterns will be recorded as measurement and used to construct the response matrices for the imaging functions.

3.2. Imaging functions. Consider an array of transmitters that can send out plane incident waves and record the far-field pattern of the scattered waves. Assume that we have a set of incident plane waves with incident directions $\mathbf{d}_1, \ldots, \mathbf{d}_N$ and the far-field patterns are recorded at observation direction $\hat{\mathbf{r}}_1, \ldots, \hat{\mathbf{r}}_M$. These measurement of the far-field patterns form an $M \times N$ response matrix P with each entry given by

$$(3.5) \qquad P_{ij} = \psi_{\infty}(\hat{\mathbf{r}}_i, \mathbf{d}_j),$$

where the far-field pattern ψ_{∞} represents any one of the far-field patterns for (3.2), (3.3), or (3.4). The response matrix can be regarded as a discrete version of the scattering operator.

Here we give some physical interpretation of the response matrix to motivate the construction of our imaging functions. First, from the observation point of view, the scattered far field pattern can be viewed as the superposition of far field pattern of point scatterers distributed (with the total field ϕ as the weight function) at locations where scattering occurs, i.e., at the point scatterers as well as at the boundary of extended scatterers based on equation (3.4). Although this interpretation sounds similar to Born approximation, which simply replaces the

total field in (3.4) by the incidence field, here we try not to assume or use explicit quantitative knowledge of the total field in the direct imaging algorithm. In the discrete setting,

$$P_{ij} = \psi_\infty(\hat{\mathbf{r}}_i, \mathbf{d}_j)$$
$$= \gamma \left[\sum_{k=1}^m \sigma_k \phi_k(\mathbf{d}_j) e^{-i\kappa\hat{\mathbf{r}}_i \cdot \mathbf{r}_k} - \int_\Gamma \partial_{\mathbf{n}'} \phi(\mathbf{r}'; \mathbf{d}_j) e^{-i\kappa\hat{\mathbf{r}}_i \cdot \mathbf{r}'} ds(\mathbf{r}') \right],$$

which means the column space of the response matrix is a subspace of the space spanned by the illumination vectors with respect to the observation array/directions

$$\mathbf{g}_r(\mathbf{r}) = (e^{-i\kappa\mathbf{r}\cdot\hat{\mathbf{r}}_1}, \ldots, e^{-i\kappa\mathbf{r}\cdot\hat{\mathbf{r}}_M})^\top, \ \mathbf{r} \in \{\mathbf{r}_1, \ldots, \mathbf{r}_m\} \cup \Gamma.$$

If we introduce far field pattern of the Green's function $G_\infty(\hat{\mathbf{r}}, \mathbf{r})$, which is the far field pattern of the scattered wave due to a point source at $\mathbf{r}$ with presence of both point and extended scatterers that can be defined by a generalized Foldy–Lax formulation similar to the one we defined for the total field (2.21) and (2.22). Then we can rewrite far field pattern for the scattered field for an incident wave $e^{i\kappa\mathbf{r}\cdot\mathbf{d}}$ as

$$(3.6) \qquad \psi_{\infty,\,\mathrm{GFL}}(\hat{\mathbf{r}}, \mathbf{d}) = \sum_{k=1}^m G_\infty(\hat{\mathbf{r}}, \mathbf{r}_k) e^{i\kappa\mathbf{r}_k\cdot\mathbf{d}} - \int_\Gamma \partial_{\mathbf{n}'} G_\infty(\hat{\mathbf{r}}, \mathbf{r}') e^{i\kappa\mathbf{r}'\cdot\mathbf{d}} ds(\mathbf{r}').$$

From the incident point of view, we can view the far field pattern as superposition of scattered wave excited at point scatterers and extended scatterer boundary by incident wave $e^{i\kappa\mathbf{r}\cdot\mathbf{d}}$, although we do not know the weight function G_∞. In the discrete setting,

$$P_{ij} = \psi_\infty(\hat{\mathbf{r}}_i, \mathbf{d}_j)$$
$$= \sum_{k=1}^m G_\infty(\hat{\mathbf{r}}_i, \mathbf{r}_k) e^{i\kappa\mathbf{r}_k\cdot\mathbf{d}_j} - \int_\Gamma \partial_{\mathbf{n}'} G_\infty(\hat{\mathbf{r}}_i, \mathbf{r}') e^{i\kappa\mathbf{r}'\cdot\mathbf{d}_j} ds(\mathbf{r}'),$$

which means the row space of the response matrix is a subspace of the space spanned by the illumination vectors with respect to the incident directions

$$\mathbf{g}_t(\mathbf{r}) = (e^{i\kappa\mathbf{r}\cdot\mathbf{d}_1}, \ldots, e^{i\kappa\mathbf{r}\cdot\mathbf{d}_N})^\top, \ \mathbf{r} \in \{\mathbf{r}_1, \ldots, \mathbf{r}_m\} \cup \Gamma.$$

In general, the knowledge of the incident wave and/or observation point gives a good clue on the form of illumination vector one should use to approximate the row and/or column space of the response matrix. How well the column or the row space can approximate the space of $\mathbf{g}_r(\mathbf{r})$ or $\mathbf{g}_t(\mathbf{r})$ respectively for $\mathbf{r} \in \{\mathbf{r}_1, \ldots, \mathbf{r}_m\} \cup \Gamma$ depends on the wavenumber κ , the sampling of incident directions $\mathbf{d}_1, \ldots, \mathbf{d}_N$ and the far-field observation directions $\hat{\mathbf{r}}_1, \ldots, \hat{\mathbf{r}}_M$, and the geometry. For discrete point scatterers whose number is fewer than $\min(M, N)$, the two spaces are the same. In general, for a point $\mathbf{r} \in \{\mathbf{r}_1, \ldots, \mathbf{r}_m\} \cup \Gamma$ that is well illuminated by the incident waves and well observed by the receiver array, $\mathbf{g}_r(\mathbf{r})$ and $\mathbf{g}_t(\mathbf{r})$ have a strong signature in the column space and row space respectively. Highly concave part of the obstacle boundary often can not be well illuminated or observed.

Now we turn the imaging problem into finding the location where scattering happens as the following. The motivation is: at each point $\mathbf{r}$ in the imaging domain, how well $\mathbf{g}_r(\mathbf{r})$ and $\mathbf{g}_t(\mathbf{r})$ are approximated by the significant component of column and row space of the response matrix respectively. First, compute the singular

value decomposition (SVD) of the response matrix (3.5).

$$P = \sum_{k=1}^{\min(M,N)} \lambda_k \mathbf{u}_k \overline{\mathbf{v}}_k^\top,$$

where $\mathbf{u}_k$ and $\mathbf{v}_k$ are the unit left and right singular vectors, and λ_k are the singular values of P. This matrix factorization turns imaging passive targets into imaging active sources with respect to the receiver and transmitter array since $\mathbf{u}_k$ and $\mathbf{v}_k$ form the orthogonal basis for the column and row spaces respectively with λ_k being the signal strength. The following quantity measures projections in each pair of left and right singular vectors $\mathbf{u}_k$ and $\mathbf{v}_k$:

$$(3.7) \qquad I_k(\mathbf{r}) = \left[\hat{\mathbf{g}}_r^\top(\mathbf{r}) \cdot \mathbf{u}_k\right] \left[\overline{\hat{\mathbf{g}}}_t^\top(\mathbf{r}) \cdot \overline{\mathbf{v}}_k\right],$$

where the $\hat{\mathbf{g}}_t$ and $\hat{\mathbf{g}}_r$ are the normalized illumination vectors with respect to the transmitter and the receiver, given explicitly as

$$\hat{\mathbf{g}}_r(\mathbf{r}) = \frac{1}{\sqrt{M}}(e^{i\kappa\mathbf{r}\cdot\hat{\mathbf{r}}_1}, \ldots, e^{i\kappa\mathbf{r}\cdot\hat{\mathbf{r}}_M})^\top \quad \text{and} \quad \hat{\mathbf{g}}_t(\mathbf{r}) = \frac{1}{\sqrt{N}}(e^{i\kappa\mathbf{r}\cdot\mathbf{d}_1}, \ldots, e^{i\kappa\mathbf{r}\cdot\mathbf{d}_N})^\top.$$

This quantity removes the phase ambiguity of the SVD of the response matrix too. The two dot product terms in (3.7) is phase matching with respect to the receiver array and the transmitter array respectively. The product of these two terms is just a summation of the two phase matching. If further superposed in frequency, it becomes travel time matching with respect to the two arrays, which is the Kirchhoff migration used in geophysics context. Furthermore, it can be easily shown that

$$\left| \sum_{k=1}^{\min(M,N)} I_k(\mathbf{r}) \right| \leq 1.$$

Define

$$\lambda_{\max} = \max_{1 \leq k \leq \min(M,N)} \{\lambda_k\} \quad \text{and} \quad \eta_k = \lambda_k/\lambda_{\max}.$$

The first imaging function is defined as

$$(3.8) \qquad \mathcal{I}_1(\mathbf{r}) = \sum_{k=1}^{\min(M,N)} \eta_k I_k(\mathbf{r}),$$

where the singular values play the role of the weights and thus the regularization in the imaging function. As we mention, if further superposed in frequency, it becomes the Kirchhoff migration in geophysics context which matches the travel time between each pair of transmitter and receiver.

The second imaging function is defined as

$$(3.9) \qquad \mathcal{I}_2(\mathbf{r}) = \sum_{k=1}^{K} I_k(\mathbf{r}),$$

where the truncation number $K \leq \min(M, N)$ is a threshold of the number of significant singular vectors. For m point scatterers, then $K = m$. In general, for extended obstacles, K may depend on the size of the obstacle and physical resolution of the array, which depends on the wavenumber κ, aperture and array setup. The truncation number K can also be used as a regularization parameter that is determined by the noise level [20, 46]. We refer to Ammari et al. [1, 3] for stability and resolution analysis for these imaging functionals.

We define the following transformed imaging functions, which seem to produce better visualization results.

$$(3.10) \qquad \widetilde{\mathcal{I}}_i(\mathbf{r}) = [1 - \mathcal{I}_i(\mathbf{r})]^{-1}, \quad i = 1, 2.$$

In Section 4, all these imaging functions are demonstrated and compared for imaging the point and extended obstacle scatterers. They essentially produce the similar quality of imaging results; while the imaging function $\widetilde{\mathcal{I}}_i$ displays a little better visualization effect.

Since we transform the inverse scattering problem into an active source problem with respect to both transmitter and receiver arrays using the SVD of the response matrix, we avoid the need to estimate the total field quantitatively which becomes a nonlinear and nonlocal problem in terms of the location and shape of the scatterers. However, consequent issues related to this formulation are:

(1) Poor illumination due to partial illumination or occlusion, may cause the total field weak at certain locations. Similarly, scattering at certain locations may not be measured due to partial observation aperture. Imaging resolution at these locations will be compromised as we will see from some of the tests below.

(2) Multiple scattering information, which is implicitly embedded in the total field, is not used if one uses homogeneous Green's function as the illumination vector.

4. Numerical experiments

In this section, we present numerical examples for the inverse scattering problem, which contains both point scatterers and extended obstacle scatterers. As discussed in Section 3.2, the response matrix is based on the far-field pattern of the scattered field with row index corresponding to the observation direction $\hat{\mathbf{r}}$ and column index corresponding to the incident direction $\mathbf{d}$. To test the stability and robustness of the method, the response matrix is perturbed by multiplicative noise as

$$P_{ij}^{\mathrm{noise}} = a \operatorname{Re} P_{ij} + \mathrm{i}\, b \operatorname{Im} P_{ij},$$

where a and b are uniformly distributed random numbers in $[1 - c, 1 + c]$ with $c = 20\%$. In the computation of the imaging functions, we use those singular vectors corresponding to singular values greater than some threshold which gives robustness to noise. As we mentioned before this threshold is the only parameter here which plays the role of physical regularization that depends on the physical setup such as used frequency, desired resolution, size of the obstacle and/or number of point scatterers, as well as signal noise ratio. On the other hand, the threshold is not very sensitive and can take a range of values that render very similar results. In all of the following examples, the wavenumber κ is taken to be 4π, i.e., the wavelength is taken to be $\lambda = 2\pi/\kappa = 0.5$.

Example 1. This is a 2D example. The incident and observation directions can be represented by the incident angle α_{inc} and the observation angle α_{obs}, respectively, i.e., $\mathbf{d} = (\cos \alpha_{\mathrm{inc}}, \ \sin \alpha_{\mathrm{inc}}) \in \mathbb{S}^1$ and $\hat{\mathbf{r}} = (\cos \alpha_{\mathrm{obs}}, \ \sin \alpha_{\mathrm{obs}}) \in \mathbb{S}^1$. First, we consider the far-field pattern with full aperture data, i.e., incident angle $\alpha_{\mathrm{inc}} \in [0, 2\pi]$ and observation angle $\alpha_{\mathrm{obs}} \in [0, 2\pi]$. The size of the response matrix is 120×120, i.e., the intervals for the incident angle and observation angle are equally subdivided into 120 subintervals. In this example, we consider an extended
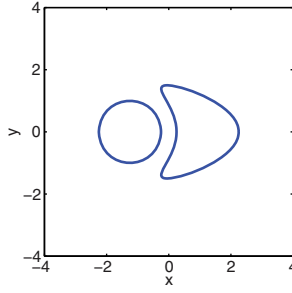
FIGURE 2. An extended obstacle scatterer with two disjoint components: one is a circle-shaped scatterer and another is kite-shaped scatterer in Example 1.
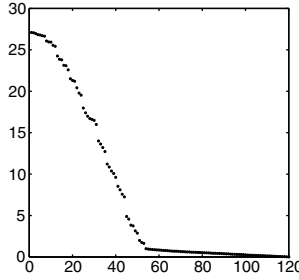

FIGURE 3. The singular value plot of the response matrix for the extended obstacle scatterers in Example 1.

obstacle scatterer with two disjoint components: one is a circle-shaped extended scatterer with the parametric representation given by

$$\mathbf{r}_1(t) = (\cos t - 1.25, \ \sin t), \quad 0 \le t \le 2\pi;$$

and another is a kite-shaped extended scatterer with the parametric representation given by

$$\mathbf{r}_2(t) = (\cos t + 0.65 \cos 2t + 0.6, \ 1.5 \sin t), \quad 0 \le t \le 2\pi,$$

as seen in Figure 2. The separation distance between these two components is only about one wavelength, which makes it hard to distinguish these two components for the imaging, especially for the concave part of the kite-shaped scatterer and the adjacent part of the circle-shaped scatterer.

Figure 3 plots the singular value pattern of the response matrix from the far-field pattern $\psi_{\infty,\mathrm{E}}$ by using the boundary integral equation for the extended obstacle scatterers. Figure 4 shows, from top to bottom and from left to right, the imaging of the two isolated extended obstacle scatterers by using imaging functions $\mathcal{I}_1, \mathcal{I}_2, \widetilde{\mathcal{I}}_1$, and $\widetilde{\mathcal{I}}_2$, respectively. It can be seen from the imaging results that all the four imaging functions essentially produce similar results, and the two modified imaging functions $\widetilde{\mathcal{I}}_i$ displays a little better result from the visualization point of view. From now on, we will use the imaging function $\widetilde{\mathcal{I}}_2$ to present the imaging results instead of showing the results from all the imaging functions.
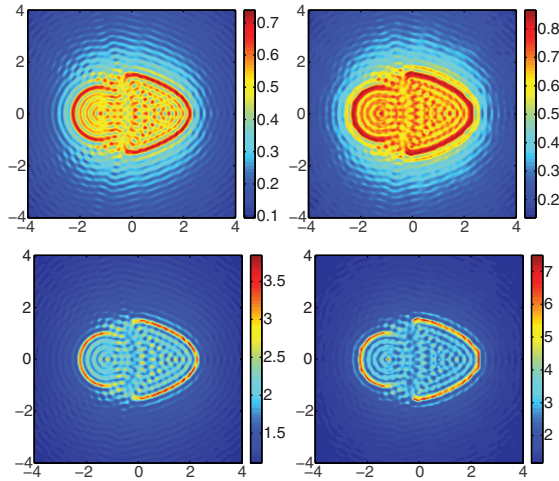
FIGURE 4. Imaging of the extended obstacle scatterers by using
the boundary integral equation in Example 1. (top left) imaging
result by $\mathcal{I}_1$; (top right) imaging result by $\mathcal{I}_2$; (bottom left) imaging
result by $\widetilde{\mathcal{I}}_1$; (bottom right) imaging result by $\widetilde{\mathcal{I}}_2$.

Next we show the imaging results from the far-field pattern with limited aper-
ture data and demonstrate that the proposed imaging method can also handle the
missing data case. We consider so-called limited back-scattered aperture data with
incident angle $\alpha_{\mathrm{inc}} \in [-\pi/2, \pi/2]$ and observation angle $\alpha_{\mathrm{obs}} \in [-\pi/2, \pi/2]$, and
limited forward-scattered aperture data with incident angle $\alpha_{\mathrm{inc}} \in [-\pi/2, \pi/2]$ and
observation angle $\alpha_{\mathrm{obs}} \in [\pi/2, 3\pi/2]$. The size of the response matrix is still the
same as the full aperture case 120×120, i.e., the intervals for the incident angle and
observation angle are also equally subdivided into 120 subintervals. Figure 5 shows
the singular value distribution of the response matrices for the far-field pattern by
using back-scattered limited aperture data and forward-scattered limited aperture
data. Based on the singular value distributions, we can make the following two
observations: (i) the extended scatterers is not a superposition of point scatterers,
i.e., each singular vector does not corresponds to a point on the boundary; (ii) the
response matrix obtained from full aperture data contains more leading singular
values and hence more information than that from limited aperture data. Figure
6 shows the imaging of the two obstacle scatterers by using back-scattered limited
aperture data and forward-scattered limited aperture data. Evidently, comparing
4 with 6, the full aperture data produces a much better result than those using
limited aperture data. The back-scattered limited aperture data yields a blurred
profile for the two extended obstacle scatterers. Using Born approximation, one
can see that back-scattered data contains mainly low frequency information of the
shape. The forward-scattered limited aperture gives a clear image of the convex
arc part of the circle-shaped obstacle, which is illuminated best by the array of
transducers.

Example 2. This example has the same two extended obstacles as Example.
Besides, the extended obstacles are surrounded by a set of 100 randomly distributed
point scatterers in an annulus with radii bounded below by 3 and above by 4, as
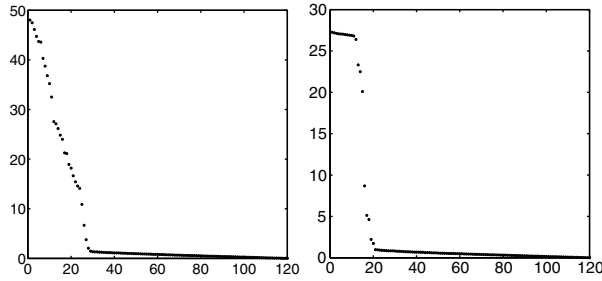
FIGURE 5. The singular value plot of the response matrices for the extended obstacle scatterers in Example 1. (left) limited back-scattered aperture data; (right) limited forward-scattered aperture data.
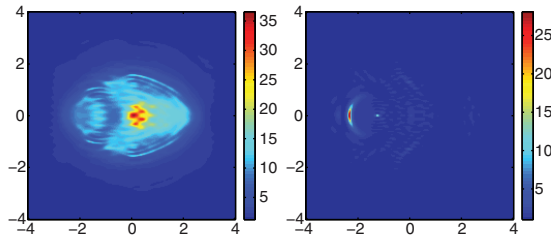

FIGURE 6. Imaging of the extended obstacle scatterers by using the boundary integral equation in Example 1. (left) limited back-scattered aperture data; (right) limited forward-scattered aperture data.
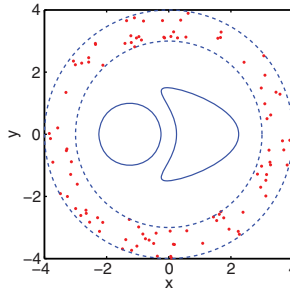

FIGURE 7. A set of one hundred of randomly distributed point scatterers in the annulus with radii bounded blow by 3 and above by 4, and an extended obstacle scatterer with two disjoint components: one is a circle-shaped scatterer and another is kite-shaped scatterer in Example 2.

seen in Figure 7. The scattering coefficient σ_j is taken as a random number from the interval $(0, 1)$ for $j = 1, \ldots, 100$. We consider the full aperture data and the size of the response matrix is 120×120.
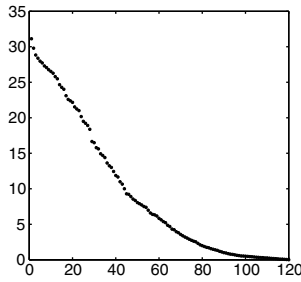
FIGURE 8. The singular value plot of the response matrix for the point and extended obstacle scatterers in Example 2.
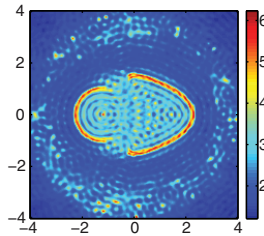

FIGURE 9. Imaging of the point and extended obstacle scatterers by using the generalized Foldy–Lax formulation by $\widetilde{\mathcal{I}}_2$ in Example 2.

Figure 8 plots the singular value pattern of the response matrix from the far-field pattern $\psi_{\infty,\mathrm{GFL}}$ by using the generalized Foldy–Lax formulation for the mixed point and extended scatterers. Figure 9 shows the imaging of the 100 randomly distributed point scatterers and two scatterers by using full aperture data and imaging function $\widetilde{\mathcal{I}}_2$. The imaging highlights not only the profile of the two extended scatterers but also the location of the point scatterers. Since the scattering coefficients are randomly chosen from the interval $(0, 1)$, they may not be all strong scatterers, which explains some point scatterers are clearly located but some are not so clearly spotted.

To investigate how each far-field pattern contributes to the overall imaging, Figure 10 shows the imaging results based on the projection method of the far-field patterns. The method of the projection is given in Appendix, which describes how to project the column space of the response matrix P_{GFL} out of the column spaces spanned by the columns of the response matrices of P_{FL} and P_{E}. Figure 10 shows, from left to right, the imaging results by using the response matrix P_1, P_2, and P_3, respectively. The left figure in Figure 10 looks like the one in Figure 4 since the 100 point scatterers are taken from the overall imaging in Figure 9. The middle figure in Figure 9 shows the imaging for the 100 randomly distributed point scatterers by taking out the contribution of the extended scatterers from the response matrix. The right figure in Figure 10 shows the imaging result arising from the multiple interaction between the point scatterers and the extended obstacle scatterers.

Example 3. This example is a three-dimensional case. The incident and observation directions can be represented by the incident angles α_{inc} and β_{inc} and
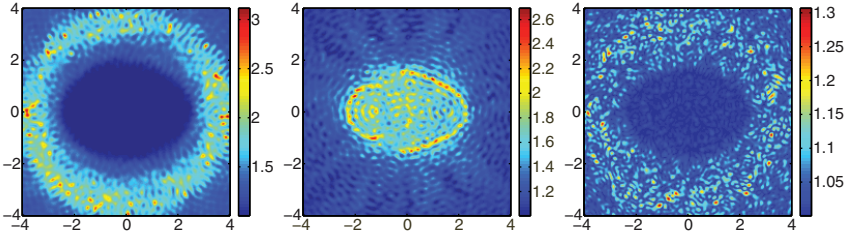
FIGURE 10. Imaging of the point and extended obstacle scatterers by using different far-field patterns in Example 2. (left) imaging from the response matrix P_1; (middle) imaging from the response matrix P_2; (right) imaging from the response matrix P_3.
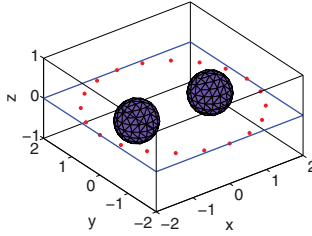

FIGURE 11. A set of twenty equally spaced point scatterers on a circle with radius 2 on the xy-plane and two spherical obstacle scatterers with centers at $(-1.0, 0.0, 0.0)$ and $(1.0, 0.0, 0.0)$ and the same radius of 0.5 in Example 3.

the observation angles α_{obs} and β_{obs}, i.e.,

$$\mathbf{d} = (\cos\alpha_{\text{inc}}\sin\beta_{\text{inc}}, \ \sin\alpha_{\text{inc}}\sin\beta_{\text{inc}}, \ \cos\beta_{\text{inc}}) \in \mathbb{S}^2,$$

$$\hat{\mathbf{r}} = (\cos\alpha_{\text{obs}}\sin\beta_{\text{obs}}, \ \sin\alpha_{\text{obs}}\sin\beta_{\text{obs}}, \ \cos\beta_{\text{obs}}) \in \mathbb{S}^2.$$

In this example, we only show the results for full aperture data, where $\alpha_{\text{inc}} \in [0, 2\pi], \beta_{\text{inc}} \in [0, \pi]$ and $\alpha_{\text{obs}} \in [0, 2\pi], \beta_{\text{obs}} \in [0, \pi]$, since the results for limited aperture data are analogous to the comparison between the full and the limited aperture data for the two-dimensional case. The size of the response matrix is 800×800, i.e., the intervals for the angles α_{inc} and α_{obs} are equally subdivided into 40, and the angles β_{inc} and β_{obs} are equally subdivided into 20.

In this example, we consider a group of twenty equally distributed point scatterers on a circle with radius 2 on the xy-plane, as seen in Figure 11. The scattering coefficients σ_j is chosen to be all equal, i.e., $\sigma_j = 1.0, j = 1, \ldots, 20$. The centers of two spherical obstacle scatterers with the same radius of 0.5 are located at $(-1.0, 0.0, 0.0)$ and $(1.0, 0.0, 0.0)$.

Figure 12 plots the singular value distribution of the response matrix of the scattered field for the point and two spherical obstacle scatterers. Figures 13 shows the imaging result for the point and two spherical obstacle scatterers on the planes defined by $z = 0$, $y = 0$, and $x = 1$, respectively. As we can see, the imaging results accurately locate the point scatterers and plot the profiles of the two spherical extended scatterers.
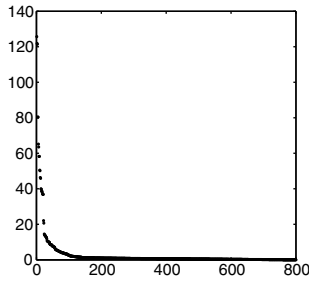
FIGURE 12. The singular value plots of the response matrix for the scattered field in Example 3.
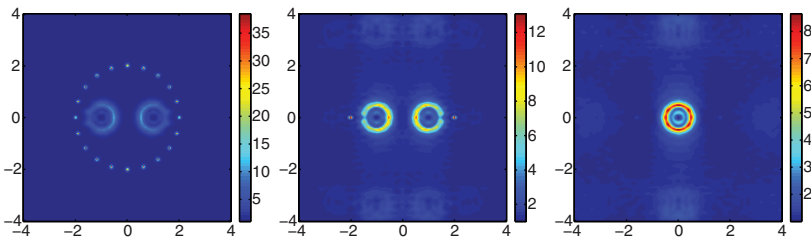

FIGURE 13. Imaging of the point and two spherical obstacle scatterers by using the Foldy–Lax formulation in Example 3. (left) slice $z = 0$; (middle) slice $y = 0$; (right) slice $x = 1$.

5. Conclusion

We use a direct imaging method to study the inverse scattering problem which contains multiple scattering between point scatterers and extended scatterers. The method is simple and efficient since no direct solver or iteration is needed, and can handle full and limited synthetic aperture data. The motivation of the problem formulation is to simulate the wave propagation and image a target in a cluttered environment, where small particles are modeled as point scatterers. A generalized Foldy–Lax formulation is used to resolve the multiple scattering between the small scale point scatterers and the extended obstacle scatterers. The direct imaging method uses the singular value decomposition of the response matrix from the far-field pattern with physically based regularization and/or thresholding to visualize the location of strong scattering. The imaging functions are robust and stable with respect to the measurement noise. In future work, we will investigate the extended obstacle scatterers with different boundary conditions, such as sound hard and mixed type of sound soft and sound hard, and the three-dimensional electromagnetic wave propagation which is governed by Maxwell's equations.

Appendix A. Orthogonal projection of response matrix

Let $\mathbf{v}_1, \ldots, \mathbf{v}_k$ be a family of orthonormal vectors in $\mathbb{C}^n$, and let

$$V = \mathrm{span}(\mathbf{v}_1, \ldots, \mathbf{v}_k).$$

Obviously, the vectors $\mathbf{v}_1, \ldots, \mathbf{v}_k$ form an orthonormal basis for the k-dimensional subspace V of $\mathbb{C}^n$. Given a vector $\mathbf{u} \in \mathbb{C}^n$, we next describe how to find the projection of the vector $\mathbf{u}$ onto the subspace V, i.e., to find a vector $\mathbf{w} \in V$ such that $\mathbf{u} - \mathbf{w} \perp V$ for all vectors in V.

Construct a $n \times k$ matrix A by using the vectors $\mathbf{v}_1, \ldots, \mathbf{v}_k$ as the columns

$$A = [\mathbf{v}_1 \cdots \mathbf{v}_k].$$

To find the project $\mathbf{w}$ onto the subspace V is equivalent to the following equation

$$A^{\mathrm{H}}(\mathbf{u} - \mathbf{w}) = 0,$$

which is equivalent to

(A.1) $$A^{\mathrm{H}}\mathbf{u} = A^{\mathrm{H}}\mathbf{w}.$$

Here H denotes the complex conjugate of the transpose. Meanwhile, since the projection $\mathbf{w}$ is on the subspace V, the vector $\mathbf{w}$ can be written as the linear combination of the vectors $\mathbf{v}_1, \ldots, \mathbf{v}_k$:

$$\mathbf{w} = x_1\mathbf{v}_1 + x_2\mathbf{v}_2 + \cdots + x_k\mathbf{v}_k = A\mathbf{x},$$

where $\mathbf{x} = (x_1 \ldots x_k)^{\top}$ is a k-dimensional column vector. Hence (A.1) can be written as

$$A^{\mathrm{H}}\mathbf{u} = A^{\mathrm{H}}A\mathbf{x}.$$

Noticing $A^{\mathrm{H}}A = I_{k \times k}$ since $\mathbf{v}_1, \ldots, \mathbf{v}_k$ are orthonormal. The above equation gives

$$\mathbf{x} = A^{\mathrm{H}}\mathbf{u},$$

which yields the projection

$$\mathbf{w} = AA^{\mathrm{H}}\mathbf{u}.$$

Let $Q = AA^{\mathrm{H}}$. The matrix Q is called the projection matrix for the subspace V.

Define the response matrix

$$P_{ij} = \psi_{\infty}(\hat{\mathbf{r}}_i, \mathbf{d}_j),$$

where ψ_{∞} is the far-field pattern, $\mathbf{r}_i$ is the observation direction vector, and $\mathbf{d}_j$ is the incident direction vector. For convenience, we introduce three response matrices $P_{\mathrm{FL}}, P_{\mathrm{E}}$, and P_{GFL}, which stand for the response matrix for the point scatterers, extended obstacle, and mixed scatterers with both point scatterers and extended obstacle, respectively.

Next we describe how to project the columns of the response matrix P_{GFL} out of the response matrix P_{FL} and/or the response matrix P_{E}. We can do the SVD for P_{FL} and P_{E}, and pick the set of leading left singular vectors $\mathbf{u}_1, \ldots, \mathbf{u}_m$ and $\mathbf{v}_1, \ldots, \mathbf{v}_n$ from the SVD of P_{FL} and P_{E}, respectively. Using these orthonormal vectors, we can construct

$$A_{\mathrm{FL}} = (\mathbf{u}_1 \ldots \mathbf{u}_m)$$

and

$$A_{\mathrm{E}} = (\mathbf{v}_1 \ldots \mathbf{v}_n).$$

Then we can construct the project matrices

$$Q_{\mathrm{FL}} = A_{\mathrm{FL}}A_{\mathrm{FL}}^{\mathrm{H}}$$

and

$$Q_{\mathrm{E}} = A_{\mathrm{E}}A_{\mathrm{E}}^{\mathrm{H}}.$$

Finally we can study the projection of the response matrix P_{GFL}:

$$(A.2) \qquad P_1 = P_{\text{GFL}} - Q_{\text{E}} P_{\text{GFL}} = (I - Q_{\text{E}}) P_{\text{GFL}},$$

$$(A.3) \qquad P_2 = P_{\text{GFL}} - Q_{\text{FL}} P_{\text{GFL}} = (I - Q_{\text{FL}}) P_{\text{GFL}},$$

$$(A.4) \qquad P_3 = P_{\text{GFL}} - Q_{\text{E}} P_{\text{GFL}} - Q_{\text{FL}} P_{\text{GFL}} = (I - Q_{\text{E}} - Q_{\text{FL}}) P_{\text{GFL}}.$$

The direct imaging function can be construct from the SVD of P_1, P_2, and P_3.

References

[1] Habib Ammari, Josselin Garnier, Hyeonbae Kang, Mikyoung Lim, and Knut Sølna, *Multistatic imaging of extended targets*, SIAM J. Imaging Sci. **5** (2012), no. 2, 564–600, DOI 10.1137/10080631X. MR2971173

[2] *Mathematical and statistical methods for imaging*, Contemporary Mathematics, vol. 548, American Mathematical Society, Providence, RI, 2011. Papers from the NIMS Thematic Workshop held at Inha University, Incheon, August 10–13, 2010; Edited by Habib Ammari, Josselin Garnier, Hyeonbae Kang and Knut Sølna. MR2868483 (2012h:65006)

[3] Habib Ammari, Hyeonbae Kang, Eunjoo Kim, Mikyoung Lim, and Kaouthar Louati, *A direct algorithm for ultrasound imaging of internal corrosion*, SIAM J. Numer. Anal. **49** (2011), no. 3, 1177–1193, DOI 10.1137/100784710. MR2812563 (2012m:65386)

[4] Gang Bao, Songming Hou, and Peijun Li, *Inverse scattering by a continuation method with initial guesses from a direct imaging algorithm*, J. Comput. Phys. **227** (2007), no. 1, 755–762, DOI 10.1016/j.jcp.2007.08.020. MR2361544 (2008h:65038)

[5] G. Bao, S. Hou, and P. Li, *Recent studies on inverse medium scattering problems*, Modeling and computations in electromagnetics, Lect. Notes Comput. Sci. Eng. vol. 59, Springer, Berlin, 2008, pp. 165–186, DOI 10.1007/978-3-540-73778-0_6. MR2766829 (2012f:78011)

[6] Fioralba Cakoni and David Colton, *Qualitative methods in inverse scattering theory*, Interaction of Mechanics and Mathematics, Springer-Verlag, Berlin, 2006. An introduction. MR2256477 (2008c:35334)

[7] Margaret Cheney, *The linear sampling method and the MUSIC algorithm*, Inverse Problems **17** (2001), no. 4, 591–595, DOI 10.1088/0266-5611/17/4/301. Special issue to celebrate Pierre Sabatier's 65th birthday (Montpellier, 2000). MR1861470

[8] J. Cheng, J. J. Liu, and G. Nakamura, *The numerical realization of the probe method for the inverse scattering problems from the near-field data*, Inverse Problems **21** (2005), no. 3, 839–855, DOI 10.1088/0266-5611/21/3/004. MR2144808 (2006b:35335)

[9] Yves Colin de Verdière, *Pseudo-laplaciens. I* (French, with English summary), Ann. Inst. Fourier (Grenoble) **32** (1982), no. 3, xiii, 275–286. MR688031 (84k:58221)

[10] David Colton, Joe Coyle, and Peter Monk, *Recent developments in inverse acoustic scattering theory*, SIAM Rev. **42** (2000), no. 3, 369–414, DOI 10.1137/S0036144500367337. MR1786932 (2001f:76066)

[11] David Colton and Andreas Kirsch, *A simple method for solving inverse scattering problems in the resonance region*, Inverse Problems **12** (1996), no. 4, 383–393, DOI 10.1088/0266-5611/12/4/003. MR1402098 (97d:35032)

[12] David L. Colton and Rainer Kress, *Integral equation methods in scattering theory*, Pure and Applied Mathematics (New York), John Wiley & Sons Inc. New York, 1983. A Wiley-Interscience Publication. MR700400 (85d:35001)

[13] David Colton and Rainer Kress, *Inverse acoustic and electromagnetic scattering theory*, 2nd ed. Applied Mathematical Sciences, vol. 93, Springer-Verlag, Berlin, 1998. MR1635980 (99c:35181)

[14] A. Devaney, *Super-resolution processing of multi-static data using time-reversal and MUSIC*, J. Acoust. Soc. Am., submitted.

[15] Klaus Erhard and Roland Potthast, *A numerical study of the probe method*, SIAM J. Sci. Comput. **28** (2006), no. 5, 1597–1612 (electronic), DOI 10.1137/040607149. MR2272180 (2007h:35349)

[16] Leslie L. Foldy, *The multiple scattering of waves. I. General theory of isotropic scattering by randomly distributed scatterers*, Phys. Rev. (2) **67** (1945), 107–119. MR0011845 (6,224e)

[17] F. Gruber, E. Marengo, and A. Devaney, *Time-reversal imaging with multiple signal calssification considering multiple scattering between the targets*, J. Acoust. Soc. Am. **115** (2004), 3042–3047.

[18] Frank Hettlich, *Fréchet derivatives in inverse obstacle scattering*, Inverse Problems **11** (1995), no. 2, 371–382. MR1324650 (95k:35217)

[19] Thorsten Hohage, *Convergence rates of a regularized Newton method in sound-hard inverse scattering*, SIAM J. Numer. Anal. **36** (1999), no. 1, 125–142 (electronic), DOI 10.1137/S0036142997327750. MR1654583 (99j:65107)

[20] Songming Hou, Knut Solna, and Hongkai Zhao, *Imaging of location and geometry for extended targets using the response matrix*, J. Comput. Phys. **199** (2004), no. 1, 317–338, DOI 10.1016/j.jcp.2004.02.010. MR2081006 (2005k:78016)

[21] Songming Hou, Knut Solna, and Hongkai Zhao, *A direct imaging algorithm for extended targets*, Inverse Problems **22** (2006), no. 4, 1151–1178, DOI 10.1088/0266-5611/22/4/003. MR2249458 (2007b:78009)

[22] Songming Hou, Knut Solna, and Hongkai Zhao, *A direct imaging method using far-field data*, Inverse Problems **23** (2007), no. 4, 1533–1546, DOI 10.1088/0266-5611/23/4/010. MR2348080 (2009b:65142)

[23] S. Hou, K. Huang, K. Solna, and H. Zhao, *A phase and space coherent direct imaging method*, J. Acoust. Soc. Am. **125** (2009), 227–238.

[24] Kai Huang and Peijun Li, *A two-scale multiple scattering problem*, Multiscale Model. Simul. **8** (2010), no. 4, 1511–1534, DOI 10.1137/090771090. MR2718270 (2011k:35160)

[25] Kai Huang, Peijun Li, and Hongkai Zhao, *An efficient algorithm for the generalized Foldy-Lax formulation*, J. Comput. Phys. **234** (2013), 376–398, DOI 10.1016/j.jcp.2012.09.027. MR2999783

[26] Kai Huang, Knut Solna, and Hongkai Zhao, *Generalized Foldy-Lax formulation*, J. Comput. Phys. **229** (2010), no. 12, 4544–4553, DOI 10.1016/j.jcp.2010.02.021. MR2643662 (2011b:78011)

[27] Masaru Ikehata, *Reconstruction of an obstacle from the scattering amplitude at a fixed frequency*, Inverse Problems **14** (1998), no. 4, 949–954, DOI 10.1088/0266-5611/14/4/012. MR1642552 (99e:35242)

[28] M. Ikehata, *Reconstruction of obstacle from boundary measurements*, Wave Motion **30** (1999), no. 3, 205–223, DOI 10.1016/S0165-2125(99)00006-2. MR1708203 (2000i:35214)

[29] E. Kerbrat, C. Prada, and M. Fink, *Imaging in the presence of grain noise using the decomposition of the time reversal operator*, J. Acoust. Soc. Am. **113** (2003), 1230–1240.

[30] A. Kirsch, *The domain derivative and two applications in inverse scattering theory*, Inverse Problems **9** (1993), no. 1, 81–96. MR1203018 (93m:35182)

[31] Andreas Kirsch, *Characterization of the shape of a scattering obstacle using the spectral data of the far field operator*, Inverse Problems **14** (1998), no. 6, 1489–1512, DOI 10.1088/0266-5611/14/6/009. MR1662460 (99k:35193)

[32] Andreas Kirsch, *The MUSIC algorithm and the factorization method in inverse scattering theory for inhomogeneous media*, Inverse Problems **18** (2002), no. 4, 1025–1040, DOI 10.1088/0266-5611/18/4/306. MR1929280 (2003f:35286)

[33] Andreas Kirsch and Natalia Grinberg, *The factorization method for inverse problems*, Oxford Lecture Series in Mathematics and its Applications, vol. 36, Oxford University Press, Oxford, 2008. MR2378253 (2009k:35322)

[34] R. Kress, *Minimizing the condition number of boundary integral operators in acoustic and electromagnetic scattering*, Quart. J. Mech. Appl. Math. **38** (1985), no. 2, 323–341, DOI 10.1093/qjmam/38.2.323. MR788479 (86g:76021)

[35] Rainer Kress, *Newton's method for inverse obstacle scattering meets the method of least squares*, Inverse Problems **19** (2003), no. 6, S91–S104, DOI 10.1088/0266-5611/19/6/056. Special section on imaging. MR2036523 (2004m:65075)

[36] Rainer Kress and William Rundell, *A quasi-Newton method in inverse obstacle scattering*, Inverse Problems **10** (1994), no. 5, 1145–1157. MR1296365 (95h:65098)

[37] Rainer Kress and William Rundell, *Inverse obstacle scattering using reduced data*, SIAM J. Appl. Math. **59** (1999), no. 2, 442–454 (electronic), DOI 10.1137/S0036139997316598. MR1654431 (99h:35029)

[38] Melvin Lax, *Multiple scattering of waves*, Rev. Modern Physics **23** (1951), 287–310. MR0046273 (13,708a)

[39] P. A. Martin, *Multiple scattering*, Encyclopedia of Mathematics and its Applications, vol. 107, Cambridge University Press, Cambridge, 2006. Interaction of time-harmonic waves with N obstacles. MR2259988 (2007k:35348)

[40] Roland Potthast, *Stability estimates and reconstructions in inverse acoustic scattering using singular sources*, J. Comput. Appl. Math. **114** (2000), no. 2, 247–274, DOI 10.1016/S0377-0427(99)00201-0. MR1737077 (2000k:35297)

[41] Roland Potthast, *A new non-iterative singular sources method for the reconstruction of piecewise constant media*, Numer. Math. **98** (2004), no. 4, 703–730, DOI 10.1007/s00211-004-0524-y. MR2099318 (2006b:35346)

[42] C. Prada and J.-L. Thomas, *Experimental subwavelength localization of scatterers by decomposition of the time reversal operator interpreted as a covariance matrix*, J. Acoust. Soc. Am. **114** (2003), 235–243.

[43] Zeév Rudnick and Henrik Ueberschär, *Statistics of wave functions for a point scatterer on the torus*, Comm. Math. Phys. **316** (2012), no. 3, 763–782, DOI 10.1007/s00220-012-1556-2. MR2993932

[44] R. Schmidt, *Multiple emitter location and signal parameter estimation*, IEEE Trans. Antennas Propag. **34** (1986), 276–280.

[45] J. Sun, S. Carney, and J. Schotland, *Strong tip effects in near-field optical tomography*, J. App. Phys. **102** (2007), 103103.

[46] Hongkai Zhao, *Analysis of the response matrix for an extended target*, SIAM J. Appl. Math. **64** (2004), no. 3, 725–745, DOI 10.1137/S0036139902415282. MR2068119 (2005a:74050)

DEPARTMENT OF MATHEMATICS, ZHEJIANG UNIVERSITY, HANGZHOU 310027, CHINA AND DEPARTMENT OF MATHEMATICS, MICHIGAN STATE UNIVERSITY, EAST LANSING, MICHIGAN 48824
E-mail address: `drbaogang@gmail.com`

DEPARTMENT OF MATHEMATICS AND STATISTICS, FLORIDA INTERNATIONAL UNIVERSITY, MIAMI, FLORIDA 33199
E-mail address: `khuang@fiu.edu`

DEPARTMENT OF MATHEMATICS, PURDUE UNIVERSITY, WEST LAFAYETTE, INDIANA 47907
E-mail address: `lipeijun@math.purdue.edu`

DEPARTMENT OF MATHEMATICS, UNIVERSITY OF CALIFORNIA AT IRVINE, IRVINE, CALIFORNIA 92697
E-mail address: `zhao@math.uci.edu`